RESEARCH ARTICLE

National Science Open
2: 20220060, 2023
https://doi.org/10.1360/nso/20220060

Physics

Special Topic: Two-dimensional Materials and Devices

Real- and momentum-indirect neutral and charged excitons in a multi-valley semiconductor

Zhiheng Huang[1,2,#], Yuhui Li[1,2,#], Tao Bo[3,#], Yanchong Zhao[1,2], Fanfan Wu[1,2], Lu Li[1,2], Yalong Yuan[1,2], Yiru Ji[1,2], Le Liu[1,2], Jinpeng Tian[1,2], Yanbang Chu[1,2], Xiaozhou Zan[1,2], Yalin Peng[1,2], Xiuzhen Li[1,2], Yangkun Zhang[1,2], Kenji Watanabe[4], Takashi Taniguchi[5], Zhipei Sun[6,7], Wei Yang[1,2,8], Dongxia Shi[1,2,8], Shixuan Du[1,2,8,*], Luojun Du[1,2,8,*] & Guangyu Zhang[1,2,8,9,*]

[1]*Beijing National Laboratory for Condensed Matter Physics, Key Laboratory for Nanoscale Physics and Devices, Institute of Physics, Chinese Academy of Sciences, Beijing 100190, China;*
[2]*School of Physical Sciences, University of Chinese Academy of Sciences, Beijing 100190, China;*
[3]*Ningbo Institute of Materials Technology & Engineering, Chinese Academy of Sciences, Ningbo 315201, China;*
[4]*Research Center for Functional Materials, National Institute for Materials Science, 1-1 Namiki, Tsukuba 305-0044, Japan;*
[5]*International Center for Materials Nanoarchitectonics, National Institute for Materials Science, 1-1 Namiki, Tsukuba 305-0044, Japan;*
[6]*Department of Electronics and Nanoengineering, Aalto University, Tietotie 3, Espoo FI-02150, Finland;*
[7]*Quantum Technology Finland (QTF) Centre of Excellence, Department of Applied Physics, Aalto University, Aalto FI-00076, Finland;*
[8]*Beijing Key Laboratory for Nanomaterials and Nanodevices, Beijing 100190, China;*
[9]*Songshan Lake Materials Laboratory, Dongguan 523808, China*

#Contributed equally to this work.
*Corresponding authors (emails: sxdu@iphy.ac.cn (Shixuan Du); luojun.du@iphy.ac.cn (Luojun Du); gyzhang@iphy.ac.cn (Guangyu Zhang))

Received 30 September 2022; Revised 2 January 2023; Accepted 16 January 2023; Published online 9 June 2023

Abstract: Excitons dominate the photonic and optoelectronic properties of a material. Although significant advancements exist in understanding various types of excitons, progress on excitons that are indirect in both real- and momentum-spaces is still limited. Here, we demonstrate the real- and momentum-indirect neutral and charged excitons (including their phonon replicas) in a multi-valley semiconductor of bilayer MoS_2, by performing electric-field/doping-density dependent photoluminescence. Together with first-principles calculations, we uncover that the observed real- and momentum-indirect exciton involves electron/hole from K/Γ valley, solving the longstanding controversy of its momentum origin. Remarkably, the binding energy of real- and momentum-indirect charged exciton is extremely large (i.e., ~59 meV), more than twice that of real- and momentum-direct charged exciton (i.e., ~24 meV). The giant binding energy, along with the electrical tunability and long lifetime, endows real- and momentum-indirect excitons an emerging platform to study many-body physics and to illuminate developments in photonics and optoelectronics.

Keywords: excitons, real- and momentum-indirect exciton, giant binding energy, electrical tunability, multi-valley semiconductor

INTRODUCTION

Excitons and their complexes (e.g., phonon replicas, biexcitons, and Fermi polarons) are elementary excitations that predominate the optical properties of a material and hence underlie the development of various

emerging technological advances in photonics and optoelectronics [1]. According to the relative positions of the constituent electrons and holes in real- and momentum-spaces, excitons can be categorized into four types: real- and momentum-direct (type-I), real-direct but momentum-indirect (type-II), momentum-direct but real-indirect (type-III), and real- and momentum-indirect (type-IV), as shown in Figure 1. Type-I excitons can strongly couple to photons and show large luminescence quantum efficiency, setting a foundation for a wide variety of optoelectronic applications, such as light-emitting diodes, lasers, solar cells, and optoelectronic devices [2–5]. However, the rather short lifetime of real- and momentum-direct excitons strongly impedes their applications in scientific research and technological innovation where long-lived excitons are required, for example, exciton superfluid phase, exciton crystals, and exciton transistors [6,7].

Notably, in some intentionally designed systems, such as van der Waals heterostructures with a staggered band alignment [8–10] and quantum wells under an external electric field [11], the wave functions of the constituent electrons and holes are spatially separated, resulting in the formation of real-space indirect excitons (also referred to as interlayer excitons or spatially indirect excitons). Thanks to the spatial separation of the electrons and holes, real-space indirect excitons exhibit a much longer lifetime than the real- and momentum-direct ones [9,12–14]. In the light of the long-lived real-space indirect excitons, a wide variety of captivating physical phenomena has been demonstrated, including but not limited to exciton Bose-Einstein condensation [15–18], correlated excitonic insulator states [19–21], and dissipationless valley exciton devices [14,22]. In addition, real-space indirect excitons harbor in-built electric dipoles and are widely tunable in applied electric fields [2,9,10,23–25], representing an advantageous scenario for technological applications. Although substantial developments and progress on understanding the real-space indirect excitons have been witnessed, the studies of real-space indirect excitons have mainly focused on the momentum-bright species (i.e., type-III excitons) with electrons and holes localized in the same valley of the Brillouin zone (BZ) [9,12,14,23,26–28]. However, the real- and momentum-indirect excitons (type-IV), which are expected to possess an even longer lifetime than the momentum-direct but real-indirect ones due to the dark nature in both real- and momentum-spaces, are still largely unexplored experimentally.

A suitable candidate for investigating real- and momentum-indirect excitons should meet two basic conditions simultaneously. First, it should possess multi-valleys in conduction and valence bands, endowing the possibility of momentum-indirect excitons. Second, for Bloch states at distinct valleys, the orbital compositions should be different. Consequently, the wave functions of different valleys reside at different positions in real-space, which enables the momentum-indirect excitons to be indirect in real-space as well. In

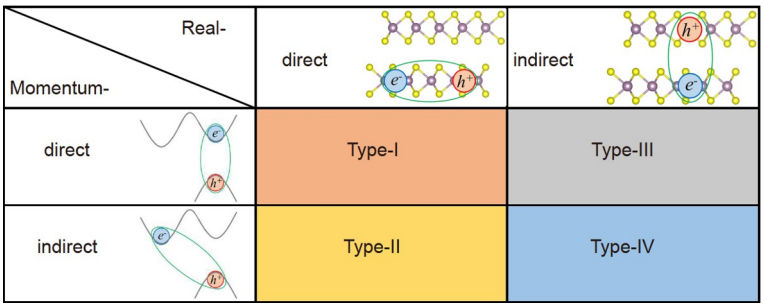

Figure 1 Real- and momentum-indirect and direct excitons. Based on the configurations of the constituent electrons and holes in real- and momentum-spaces, excitons can be divided into four types: real- and momentum-direct (type-I), real-direct but momentum-indirect (type-II), momentum-direct but real-indirect (type-III), and real- and momentum-indirect (type-IV).

particular, two-dimensional (2D) multi-valley semiconducting transition metal dichalcogenides (conduction band: Q and K valleys; valence band: K and Γ valleys) with different orbital compositions at distinct valleys provide a promising platform for real- and momentum-indirect excitons [24,25,29,30]. Despite the fact that the momentum-indirect excitons in these materials have been well uncovered [31,32], their indirect nature in real-space remains equivocal. In this work, we fabricate hexagonal boron nitride (*h*-BN) encapsulated dual-gate devices of a multi-valley semiconductor of bilayer MoS_2. Through electric-field tunable photoluminescence (PL) spectra, we identify the out-of-plane static electric dipole and quantum-confined Stark effect of momentum-indirect exciton in bilayer MoS_2, providing the smoking gun evidence of their real-space indirect characteristic and hence the existence of real- and momentum-indirect exciton. In conjunction with density functional theory (DFT) calculations, we further uncover that the observed real- and momentum-indirect exciton in bilayer MoS_2 involves electron and hole respectively from K and Γ valleys, addressing the longstanding controversy of its momentum origin. As bilayer MoS_2 is doped with electrons, new sets of PL peaks corresponding to real- and momentum-indirect charged excitons (namely trions) emerge below the energy of the real- and momentum-indirect neutral excitons. Remarkably, the binding energy of real- and momentum-indirect trion is giant in bilayer MoS_2, twice that of the real- and momentum-direct trions in transition metal dichalcogenide systems.

RESULTS AND DISCUSSION

High-quality, *h*-BN-encapsulated dual-gate bilayer MoS_2 devices (as schematically shown in Figure 2A) are fabricated by a van der Waals mediated dry-transfer method (please see Section I in Supplementary Information (SI) for more details) with few-layer graphene (FLG) as top and bottom gate electrodes. The dual-gate configuration enables us to independently tune the carrier density n_0 and out-of-plane electric field F_z. Here $n_0 = (C_bV_{bg} + C_tV_{tg}) / e$ and $F_z = (C_bV_{bg} - C_tV_{tg}) / 2\varepsilon_0\varepsilon_B$, where e is the elementary charge, ε_0 denotes the vacuum permittivity, ε_B is the out-of-plane dielectric constant of bilayer MoS_2, $C_b(V_{bg})$ and $C_t\left(V_{tg}\right)$ are the geometrical capacitances per area (applied voltages) for the bottom and top gates, respectively (details in Section IV in SI).

Figure 2B depicts the PL spectrum of device D1 at $F_z = -0.074$ V/nm. Unless otherwise specified, the data presented in the main text are taken from the high-quality device D1 in a high vacuum at 10 K with a continuous wave optical excitation at ~2.33 eV (532 nm). In addition to the well-known momentum-direct excitons, including both the real-direct transition at around 1.92 eV (labeled as X_A) and real-indirect emissions at around 1.95/2.02 eV (dubbed as IX_1/IX_2), three momentum-indirect excitons in the energy range of 1.50–1.58 eV (marked as RMX_1, RMX_2 and RMX_3, in the sequence of decreasing emission energy) can be unequivocally observed. Note that the existence of two momentum-direct but real-indirect exciton species of IX_1 and IX_2 can be ascribed to the fact that the external electric field breaks the layer degeneracy of band structure [23]. Figure 2C presents the color contour of PL spectra against the applied out-of-plane electric field F_z. To better distinguish the fine features, we extract the first-order derivative of intensity I over photon energy E ($\partial I/\partial E$) as the function of F_z, as depicted in Figure 2D. Obviously, momentum-direct but real-indirect excitons IX_1 and IX_2 vary linearly with the external electric field F_z, yet have reversed slops,

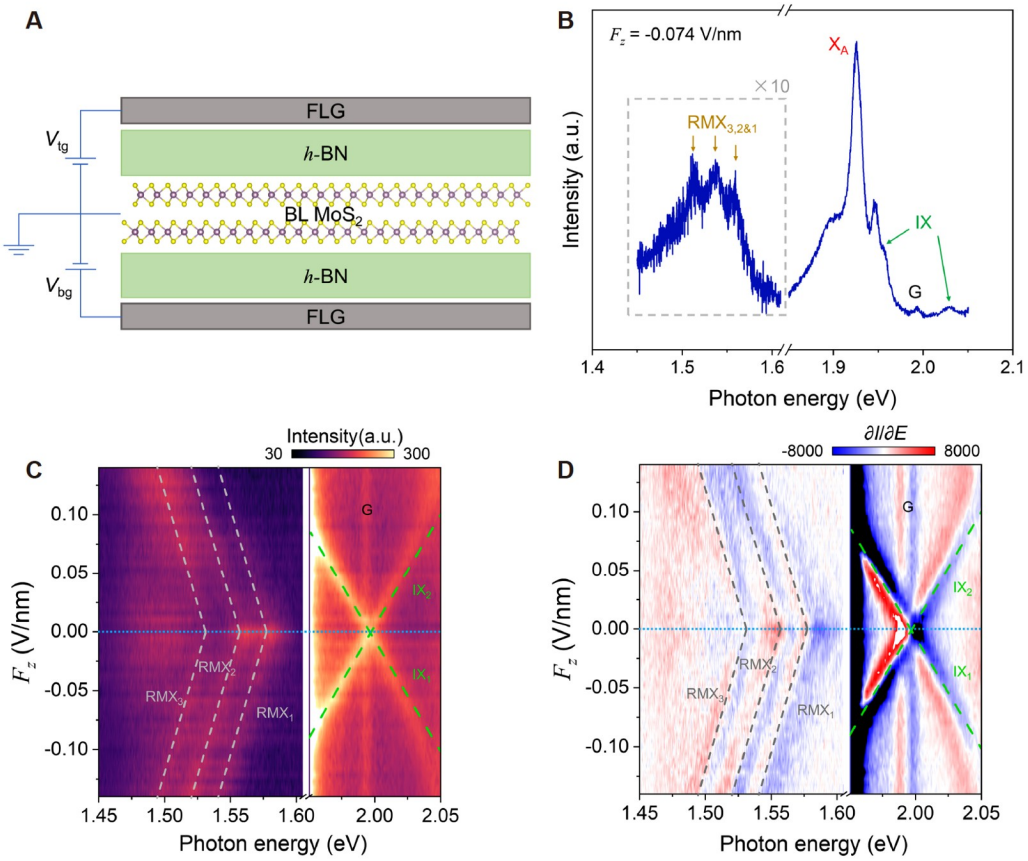

Figure 2 (A) Schematic of dual-gate *h*-BN encapsulated bilayer MoS_2 device. (B) PL spectrum of device D1 at $F_z = -0.074$ V/nm. Note that the range of 1.45–1.60 eV is magnified by 10 times for clarity. (C) Contour plot of the PL spectra of device D1 as a function of photon energy (bottom axis) and F_z (left axis). The doping density remains unchanged. (D) First-order energy derivative of (C). Real- and momentum-indirect excitons are labelled as RMX_{1-3} in the sequence of decreasing emission energy. Gray (green) dashed lines in (C) and (D) represent linear-fits of RMX_{1-3} ($IX_{1,2}$). The peak at around 1.99 eV that is insusceptible to F_z corresponds to the Raman G peak of graphene.

evidencing their opposite out-of-plane static electric dipole moments. Via linear fitting (green dashed lines in Figure 2D and section IX in SI), we extracted the out-of-plane electric dipole moments of IX_1 and IX_2: $\mu_z(IX_1) = (0.526 \pm 0.009)e$·nm and $\mu_z(IX_2) = -(0.530 \pm 0.004)e$·nm, in good agreement with the previous results [23] and our theoretical calculations (±0.578 *e*·nm, as discussed in Section VII in SI). It is noteworthy that when an enough high electric field F_z is applied, the shifts of IX_1/IX_2 deviate from a simple linear Stark shift (Figure S5). This can be understood as the strong coupling between IX_1/IX_2 and real- and momentum-direct B excitons, as demonstrated by recent experimental measurements [33] and theoretical calculations [34].

Remarkably, the three momentum-indirect excitons RMX_{1-3} in bilayer MoS_2 also vary linearly with the applied out-of-plane electric field F_z (gray dashed lines in Figure 2D), evidencing the quantum-confined Stark effect and their indirect nature in real-space. This demonstrates that RMX_{1-3} belong to real- and momentum-indirect type-IV exciton. To further confirm their indirect nature in both real- and momentum-spaces of RMX_{1-3}, we perform DFT calculations with the Perdew-Burke-Ernzerhof generalized gradient approximation for exchange-correlation interaction (Section VII in SI). Figure 3A shows the orbital-resolved band structure of bilayer MoS_2. For the valence band, its maximum is located at the center of the first BZ (i.e.,

Γ point). For the conduction band, there are two critical points (i.e., K and Q valleys) whose energies are almost degenerate. As a consequence, Q-Γ and K-Γ transitions are the two possible configurations of momentum-indirect excitons in bilayer MoS_2. Since it is difficult for conventional techniques to directly distinguish the two transitions, the exact origin of momentum-indirect excitons in bilayer MoS_2 is highly contentious. Some indicate the momentum-indirect exciton in bilayer MoS_2 to be K-Γ transition [31,35], while the others reveal that it should be Q-Γ transition [36–38]. To solve the longstanding controversy, we derive the real-space distribution of the spin-up wavefunctions at valence band Γ, and conduction band K/Q (Figures 3B–3D). For spin-down wavefunctions, the real-space distribution can be evidently acquired by time-reversal symmetry. Obviously, the spin-up wavefunction at valence band Γ is symmetrically distributed in both layers, and shows 100% interlayer hybridization (Figure 3B). In stark contrast, the spin-up wavefunction at conduction band K is only distributed in the lower layer and hence fully layer-polarized (Figure 3C). While the spin-up wavefunction at the conduction band Q shows strong delocalization, it still has a slight layer polarization (Figure 3D). Because of the various real-space distributions and interlayer hybridization at diverse valleys, the equivalent positions in real-space of wave functions at conduction band K/Q, and valence band Γ should be quite different. Quantitatively, the equivalent positions of wave functions in real-space, defined as $r_z = \int_{-\infty}^{+\infty} r\,|\varphi(r)|^2\,\mathrm{d}r$, are $r_z = -0.5t$ ($0.5t$), $-0.08t$ ($0.08t$) and 0 for spin-up (spin-down) wavefunctions at conduction band K, conduction band Q, and valence band Γ, respectively. Here, $|\varphi(r)|^2$ denotes the probability density of wavefunction $\varphi(r)$ at real-space position r, and $t = 0.615$ nm represents the interlayer distance [39]. The origin point is set at the midpoint of the constituent two layers. Consequently, both the two possible momentum-indirect transitions are real-space indirect and possess nonvanishing out-of-plane static electric dipole moments: $\mu_z(\text{K-}\Gamma) = e \cdot [r_z(\Gamma) - r_z(\text{K})] = \pm 0.5e \cdot t = \pm 0.308e \cdot \text{nm}$ for K-Γ excitons and $\mu_z(\text{Q-}\Gamma) = e \cdot [r_z(\Gamma) - r_z(\text{Q})] = \pm 0.08e \cdot t = \pm 0.049e \cdot \text{nm}$ for Q-Γ excitons, as shown in Figure 3E. On applying an external electric field F_z, the exciton energies would vary linearly due to the quantum-confined Stark effect:

$$E = E_0 - \mu_z F_z, \tag{1}$$

where E_0 is the exciton energy at zero electric field. Importantly, the experiment results of $RMX_{1\text{-}3}$ (hollows in Figure 3F) can be described perfectly by Eq. (1) using the out-of-plane static electric dipole moment of K-Γ transition (i.e., $\mu_z(\text{K-}\Gamma) = 0.308e{\cdot}\text{nm}$), as shown by solid lines in Figure 3F (please refer to Section VI in SI for more information). This clearly manifests that the constituent electrons/holes of real- and momentum-indirect $RMX_{1\text{-}3}$ originate from K/Γ valley in the BZ, solving the longstanding debate on momentum origin. It is noteworthy that the energy difference between RMX_1 and RMX_2 (RMX_3) is ~22 meV (~46 meV), which coincides with the energy of phonon mode TA(K) or ZA(K) [2TA(K) or 2ZA(K)] [40]. Thus, the RMX_1 transition is probably a kind of zero-phonon line which may be activated by defect [25], and RMX_2 and RMX_3 should correspond to the one-phonon and two-phonon replicas of RMX_1, respectively. Note that two-phonon replica RMX_3 is too weak to be distinguished at zero electric field, but exhibits an intensity comparable to or even stronger than that of RMX_1 at high electric fields (Figures 2C and 2D). This may indicate a largely enhanced electron-phonon coupling by electric fields and deserves further studies.

Finally, we study the doping-density dependent responses of real- and momentum-indirect excitons in bilayer MoS_2. Figures 4A and 4B respectively depict the contour plot and line-cuts of PL spectra as a function

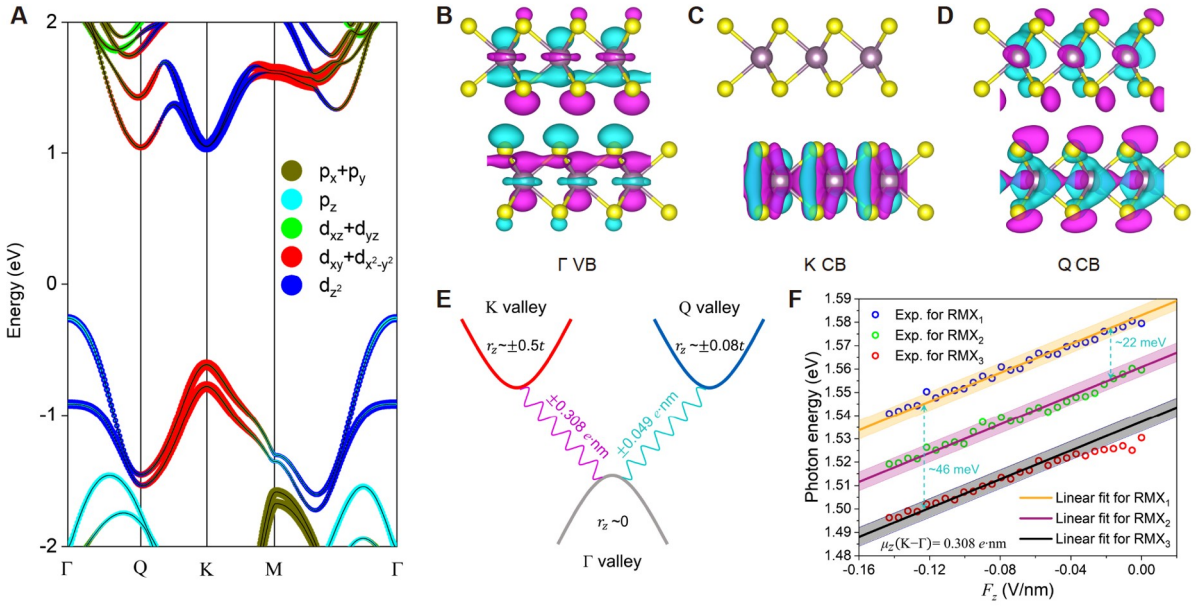

Figure 3 (A) Orbital-resolved projected band structure of bilayer MoS_2 considering the spin-orbit coupling. (B), (C), (D) Distribution of real-part of spin-up wavefunctions in real-space at valence band Γ, conduction band K, and conduction band Q, respectively. (E) Possible transition configuration for K-Γ (purple wave) and Q-Γ (cyan wave). The red (blue) curve denotes conduction band K (Q). The grey curve denotes valence band Γ. The electric dipole moment of each transition is labelled. r_z represents the equivalent position of the wavefunction at each valley as discussed in the main text. (F) Experimental results of the photon energy of RMX_1 (blue hollows), RMX_2 (green hollows) and RMX_3 (red hollows) in device D1 as a function of F_z extracted from Figure 2C. Orange, purple, black solid lines and corresponding shadow regions denote the linear-fit of $RMX_{1/2/3}$ with a fixed slope μ_z(K-Γ) obtained from DFT calculations. The energy difference between RMX_1 and RMX_2 (RMX_3) is ~22 meV (46 meV).

of doping density. Here the out-of-plane electric field F_z is fixed at zero. Remarkably, when bilayer MoS_2 is doped with electrons, new sets of PL peaks emerge below the energy of the neutral real- and momentum-indirect RMX_1 and RMX_2, which can be fitted to two new peaks with Lorentzian function (Figure 4B) and correspond to real- and momentum-indirect trions (labeled as RMT_1 and RMT_2, respectively). This is in close resemblance to the well-studied real- and momentum-direct exciton X_A, which is tuned into charged exciton (X_A^-) upon electrostatic doping [41]. Note that at F_z=0, only RMX_1 and RMX_2 can be probed (Figures 2C and 2D). Figure 4C plots the energies of RMT_1/RMT_2 and RMX_1/RMX_2 , as well as X_A/X_A^-, as a function of doping density. Notably, the binding energy of real- and momentum-indirect RMT_1 (RMT_2), i.e., the energy difference between RMX_1 (RMX_2) and RMT_1 (RMT_2), can reach up to ~59 meV (~57 meV), which is more than twice that of real- and momentum-direct X_A^- (~24 meV) in bilayer MoS_2 and also larger than the state-of-the-art results of previously reported trion in 2D semiconductors [42–45].

CONCLUSION

In short, we demonstrate the real- and momentum-indirect neutral/charged excitons (including their phonon replicas) in a multi-valley semiconductor of bilayer MoS_2 by the combination of electric-field/doping-density tunable PL measurements and first-principles calculations. Because of the sizable in-built electric dipoles, real- and momentum-indirect excitons present quantum-confined Stark effect and are widely tunable in

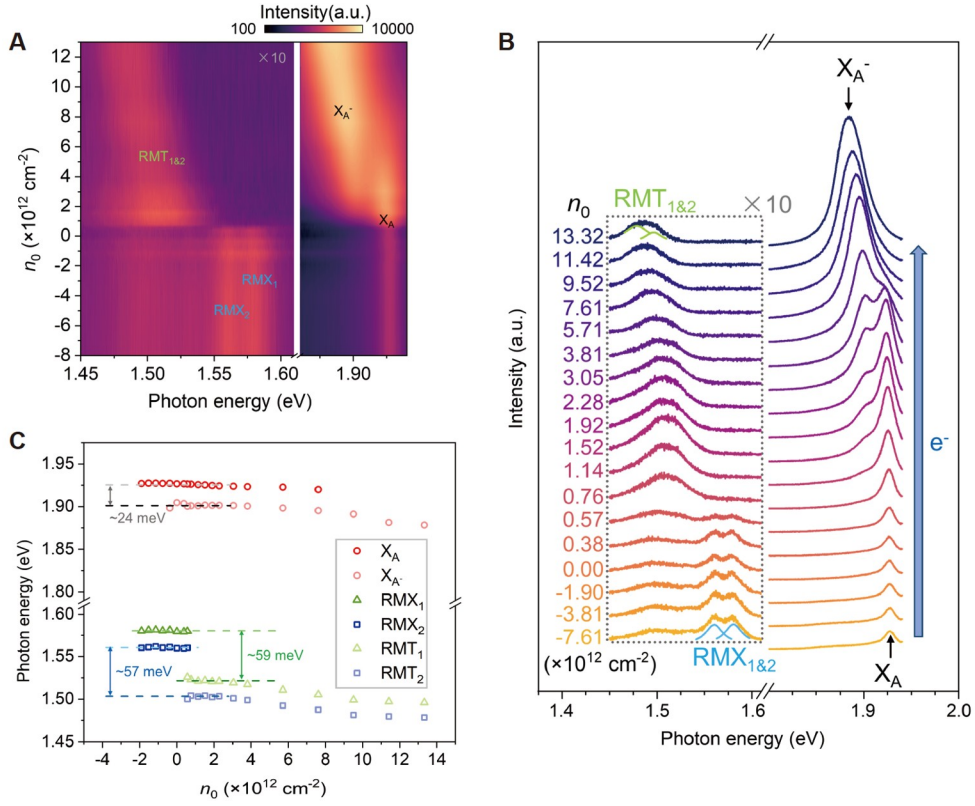

Figure 4 (A) Contour plot of the PL spectra of device D1 as a function of photon energy (bottom axis) and n_0 (left axis). The out-of-plane electric field F_z is fixed at zero. (B) PL spectra at diverse n_0. Cyan and green peaks represent Lorentz-fit peaks for $RMX_{1\&2}$ and $RMT_{1\&2}$, respectively. Note that the range of 1.45–1.60 eV in both (A) and (B) are magnified by 10 times for clarity. Offset is set in (B) for better resolution. (C) Lorentz-fitted results extracted from (B) of X_A (red hollows), X_A^- (carmine hollows), RMX_1 (green triangles), RMX_2 (blue cubes), RMT_1 (light green triangles) and RMT_2 (light blue cubes). The binding energy of X_A^-, RMT_1 and RMT_2 is approximately 24, 59 and 57 meV, respectively.

applied electric fields. Moreover, the Coulomb interaction between real- and momentum-indirect excitons and free carriers is astonishingly strong in bilayer MoS_2, endowing the giant binding energy of real- and momentum-indirect trion of ~59 meV, more than twice that of real- and momentum-direct trion (i.e., ~24 meV). Our work not only fulfills the knowledge on real- and momentum-indirect neutral and charged excitons, but also sheds light on the understanding and engineering of many-body physics and optoelectronics based on multi-valley semiconductors.

Data availability

All data needed to evaluate the conclusions are presented in the paper and/or the Supplementary Information. Additional data related to this paper may be requested from the authors.

Funding

This work was supported by the National Natural Science Foundation of China (NSFC) (12274447, 61888102, 11834017, 61734001, and 12074412), the National Key Research and Development Program (2021YFA1202900 and 2021YFA1400502), the Strategic Priority Research Program of Chinese Academy of Sciences (XDB30000000), and the Key-Area Research and Development Program of Guangdong Province (2020B0101340001).

Author contributions

G.Z. and L.D. supervised this work; L.D. and Z.H. conceived the project and designed the experiments; Z.H. fabricated the devices with the assistance from J.T., Y.C., X.Z., Y.P., X.L. and Y.Z., and carried out the optical measurements with the help of F.W; Z.H. conducted AFM measurements with the help of L.L., Y.Y. and Y.J; Y.L. under the supervision of S.D. and T.B. conducted the DFT calculations; K.W. and T.T. provided high-quality *h*-BN crystals; Z.H. and L.D. analyzed the data; Y.Z. , L. L., W.Y., D.S. and Z.S. helped with data analysis; Z.H., Y.L., L.D. and G.Z. co-wrote the manuscript. All authors discussed the results and commented on the paper.

Conflict of interest

The authors declare no conflict of interest.

Supplementary information

The Supporting Information is available free of charge at https://doi.org/10.1360/nso/20220060. The supporting materials are published as submitted, without typesetting or editing. The responsibility for scientific accuracy and content remains entirely with the authors.

References

1 Wang G, Chernikov A, Glazov MM, *et al.* Colloquium: Excitons in atomically thin transition metal dichalcogenides. *Rev Mod Phys* 2018; **90**: 021001.
2 Mak KF, Shan J. Photonics and optoelectronics of 2D semiconductor transition metal dichalcogenides. *Nat Photon* 2016; **10**: 216–226.
3 Withers F, Del Pozo-Zamudio O, Mishchenko A, *et al.* Light-emitting diodes by band-structure engineering in van der Waals heterostructures. *Nat Mater* 2015; **14**: 301–306.
4 Wu S, Buckley S, Schaibley JR, *et al.* Monolayer semiconductor nanocavity lasers with ultralow thresholds. *Nature* 2015; **520**: 69–72.
5 Baugher BWH, Churchill HOH, Yang Y, *et al.* Optoelectronic devices based on electrically tunable p-n diodes in a monolayer dichalcogenide. *Nat Nanotech* 2014; **9**: 262–267.
6 Ciarrocchi A, Tagarelli F, Avsar A, *et al.* Excitonic devices with van der Waals heterostructures: valleytronics meets twistronics. *Nat Rev Mater* 2022; **7**: 449–464.
7 Chakraborty SK, Kundu B, Nayak B, *et al.* Challenges and opportunities in 2D heterostructures for electronic and optoelectronic devices. *iScience* 2022; **25**: 103942.
8 Jin C, Ma EY, Karni O, *et al.* Ultrafast dynamics in van der Waals heterostructures. *Nat Nanotech* 2018; **13**: 994–1003.
9 Rivera P, Yu H, Seyler KL, *et al.* Interlayer valley excitons in heterobilayers of transition metal dichalcogenides. *Nat Nanotech* 2018; **13**: 1004–1015.
10 Mak KF, Shan J. Opportunities and challenges of interlayer exciton control and manipulation. *Nat Nanotech* 2018; **13**: 974–976.
11 Islam MN, Hillman RL, Miller DAB, *et al.* Electroabsorption in GaAs/AlGaAs coupled quantum well waveguides. *Appl Phys Lett* 1987; **50**: 1098–1100.
12 Rivera P, Schaibley JR, Jones AM, *et al.* Observation of long-lived interlayer excitons in monolayer $MoSe_2$-WSe_2 heterostructures. *Nat Commun* 2015; **6**: 6242.
13 Miller B, Steinhoff A, Pano B, *et al.* Long-lived direct and indirect interlayer excitons in van der Waals heterostructures. *Nano Lett* 2017; **17**: 5229–5237.
14 Jauregui LA, Joe AY, Pistunova K, *et al.* Electrical control of interlayer exciton dynamics in atomically thin heterostructures. *Science* 2019; **366**: 870–875.

15 Wang Z, Rhodes DA, Watanabe K, *et al.* Evidence of high-temperature exciton condensation in two-dimensional atomic double layers. *Nature* 2019; **574**: 76–80.

16 Li JIA, Taniguchi T, Watanabe K, *et al.* Excitonic superfluid phase in double bilayer graphene. *Nat Phys* 2017; **13**: 751–755.

17 Fogler MM, Butov LV, Novoselov KS. High-temperature superfluidity with indirect excitons in van der Waals heterostructures. *Nat Commun* 2014; **5**: 4555.

18 Liu X, Watanabe K, Taniguchi T, *et al.* Quantum Hall drag of exciton condensate in graphene. *Nat Phys* 2017; **13**: 746–750.

19 Ma L, Nguyen PX, Wang Z. Strongly correlated excitonic insulator in atomic double layers. *Nature* 2021; **598**: 585–589.

20 Zhang Z, Regan EC, Wang D. Correlated interlayer exciton insulator in heterostructures of monolayer WSe_2 and Moiré WS_2/WSe_2. *Nat Phys* 2022; **18**: 1214–1220.

21 Chen D, Lian Z, Huang X. Excitonic insulator in a heterojunction moiré superlattice. *Nat Phys* 2022; **18**: 1171–1176.

22 Unuchek D, Ciarrocchi A, Avsar A, *et al.* Room-temperature electrical control of exciton flux in a van der Waals heterostructure. *Nature* 2018; **560**: 340–344.

23 Zhao Y, Du L, Yang S, *et al.* Interlayer exciton complexes in bilayer MoS_2. *Phys Rev B* 2022; **105**: L041411.

24 Huang Z, Zhao Y, Bo T, *et al.* Spatially indirect intervalley excitons in bilayer WSe_2. *Phys Rev B* 2022; **105**: L041409.

25 Altaiary MM, Liu E, Liang CT, *et al.* Electrically switchable intervalley excitons with strong two-phonon scattering in bilayer WSe_2. *Nano Lett* 2022; **22**: 1829–1835.

26 Rivera P, Seyler KL, Yu H, *et al.* Valley-polarized exciton dynamics in a 2D semiconductor heterostructure. *Science* 2016; **351**: 688–691.

27 Arora A, Drüppel M, Schmidt R, *et al.* Interlayer excitons in a bulk van der Waals semiconductor. *Nat Commun* 2017; **8**: 639.

28 Jin C, Regan EC, Wang D, *et al.* Identification of spin, valley and moiré quasi-angular momentum of interlayer excitons. *Nat Phys* 2019; **15**: 1140–1144.

29 Liu GB, Xiao D, Yao Y, *et al.* Electronic structures and theoretical modelling of two-dimensional group-VIB transition metal dichalcogenides. *Chem Soc Rev* 2015; **44**: 2643–2663.

30 Sung J, Zhou Y, Scuri G, *et al.* Broken mirror symmetry in excitonic response of reconstructed domains in twisted $MoSe_2/MoSe_2$ bilayers. *Nat Nanotechnol* 2020; **15**: 750–754.

31 Du L, Zhang T, Liao M. Temperature-driven evolution of critical points, interlayer coupling, and layer polarization in bilayer MoS_2. *Phys Rev B* 2017; **97**: 165410.

32 Chen P, Cheng C, Shen C. Band evolution of two-dimensional transition metal dichalcogenides under electric fields. *Appl Phys Lett* 2019; **115**: 083104.

33 Leisgang N, Shree S, Paradisanos I, *et al.* Giant Stark splitting of an exciton in bilayer MoS_2. *Nat Nanotechnol* 2020; **15**: 901–907.

34 Sponfeldner L, Leisgang N, Shree S, *et al*. Capacitively-coupled and inductively-coupled excitons in bilayer MoS_2. arXiv: 2108.04248, 2021.

35 Ud Din N, Turkowski V, Rahman TS. Ultrafast charge dynamics and photoluminescence in bilayer MoS_2. *2D Mater* 2021; **8**: 025018.

36 Zhao W, Ribeiro RM, Toh M, *et al.* Origin of indirect optical transitions in few-layer MoS_2, WS_2, and WSe_2. *Nano Lett* 2013; **13**: 5627–5634.

37 Kozawa D, Kumar R, Carvalho A, *et al.* Photocarrier relaxation pathway in two-dimensional semiconducting transition metal dichalcogenides. *Nat Commun* 2014; **5**: 4543.

38 Hong J, Li K, Jin C, *et al.* Layer-dependent anisotropic electronic structure of freestanding quasi-two-dimensional MoS_2. *Phys Rev B* 2016; **93**: 075440.

39 Wakabayashi N, Smith HG, Nicklow RM. Lattice dynamics of hexagonal MoS_2 studied by neutron scattering. *Phys Rev*

B 1975; **12**: 659–663.

40 Bhatnagar M, Woźniak T, Kipczak Ł, *et al*. Temperature induced modulation of resonant Raman scattering in bilayer 2H-MoS_2. arXiv: 2204.09034, 2022.

41 Mak KF, He K, Lee C, *et al.* Tightly bound trions in monolayer MoS_2. *Nat Mater* 2013; **12**: 207–211.

42 Ross JS, Wu S, Yu H, *et al.* Electrical control of neutral and charged excitons in a monolayer semiconductor. *Nat Commun* 2013; **4**: 1474.

43 Zhu B, Chen X, Cui X. Exciton binding energy of monolayer WS_2. *Sci Rep* 2015; **5**: 9218.

44 Liu HJ, Jiao L, Xie L, *et al.* Molecular-beam epitaxy of monolayer and bilayer WSe_2: a scanning tunneling microscopy/spectroscopy study and deduction of exciton binding energy. *2D Mater* 2015; **2**: 034004.

45 Jones AM, Yu H, Ghimire NJ, *et al.* Optical generation of excitonic valley coherence in monolayer WSe_2. *Nat Nanotech* 2013; **8**: 634–638.